

Vortex beams with tunable "all-with-visible-light" dye-doped liquid crystal q-plates for broadband application

Adrián Moya*,¹ Adriana R. Sánchez-Montes,¹ Sergi Gallego,^{1,2} Eva M. Calzado,^{1,2} Andrés Márquez,^{1,2} Inmaculada Pascual,^{1,3} and Augusto Beléndez^{1,2}

¹*Instituto Universitario de Física Aplicada a las Ciencias y las Tecnologías, Universidad de Alicante, E-03080 Alicante, Spain.*

²*Departamento de Física, Ingeniería de Sistemas y Teoría de la Señal, Universidad de Alicante, E-03080 Alicante, Spain.*

³*Departamento de óptica, Farmacología y Anatomía, Universidad de Alicante, E-03080, Alicante, Spain.*

(*Electronic mail: adrian.moya@ua.es)

(Dated: 11 March 2026)

The photoalignment technique for liquid crystal (LC) device fabrication, despite being a well-established method, remains of significant relevance because of its broad applicability. Among its applications, one of particular interest is the generation of structured light, specifically the manufacturing of Pancharatman-Berry (PB) devices, capable of generating optical vortices with angular momentum. In this work, we propose a thorough theoretical and experimental analysis of the optical response of dye-doped liquid crystal (DDLDC) devices by examining their performance in terms of tunability and achromaticity across the whole visible spectrum, considering diattenuation effects and how they affect the efficiency of the devices. We experimentally demonstrate the fabrication of photoaligned devices in the visible range with 532 nm laser light and the robust generation of high-quality optical vortices, achieved by a straightforward and accessible technique using a commercial Variable Spiral Plate (VSP), avoiding the need for complex rotational systems or programmable spatial light modulators. Our results demonstrate that diattenuation effects do not prevent the functionality of the devices across the whole visible spectrum and with extended ranges of achromaticity.

I. INTRODUCTION

The photoalignment technique has become a key method for orienting Liquid Crystal (LC) molecules¹⁻³ without physical contact, offering benefits over traditional rubbing techniques^{4,5}, such as the elimination of permanent substrate surface modifications and potential contamination. Other alternatives, such as nanoparticle alignment⁶ and surface topography-induced alignment of LCs^{7,8} among others⁹, have been proposed over the years. Phototalignment is a non-invasive approach that enables precise local control over LC alignment with the exclusive use of light, facilitating the fabrication of advanced photonic devices. Recent advancements have expanded the applicability of photoalignment in areas like spatial light modulators^{10,11}, rewritable liquid-crystal- alignment technology¹², optical switches¹³, diffraction gratings¹⁴, Fresnel lenses¹⁵, etc, demonstrating the versatility of this technique in modern photonic applications. A very appealing application which can take full advantage of photoalignment technologies is the generation of structured light, where a thorough modelling of interplay between retardation and diattenuation might widen the scope of fabrication approaches, as we will show in the paper.

Structured light generation is an area of modern optics with a lot of potential¹⁶⁻¹⁸, where liquid crystals have proven essential in producing beams with complex polarization states, such as radial and azimuthal polarizations. These polarization states are characterised by their distinct electric field distributions, which are advantageous in applications like high-resolution microscopy^{19,20}, image edge enhancement²¹, optical trapping^{22,23}, optical communications²⁴ and optical sensing²⁵, among others. The ability to produce beams of

this type has been demonstrated using LC-based devices such as Pancharatnam-Berry (PB) optical devices^{26,27}, Spiral Phase Plates²⁸, q-plates^{29,30} or Liquid Crystal on Silicon spatial light modulators (LCoS)³¹⁻³³, enabled by the anisotropic properties of LCs to manipulate the properties of light. Furthermore, photoalignment techniques make it possible to manufacture devices capable of producing structured light output by local and tunable modulation of a polarized beam, enabling the generation of structured light with high efficiency^{34,35}. Depending on the physical principle, large ranges of achromaticity can be obtained in the generation of structured beams, as when illuminating PB devices with broadband light. However, a full exploration of the combination of achromaticity and tunability with diattenuation phenomena still needs to be undertaken.

The photoalignment technique using azo dyes is based on the photoisomerization mechanism of azobenzene derivatives, which undergo a reversible cis-trans transformation upon exposure to polarized light. When a layer doped with an azo dye is illuminated with linearly polarized light, the dye molecules reorient themselves perpendicularly to the polarization direction. The reorientation of adjacent LC molecules is induced by surface anchoring forces¹⁻³. Some compounds, like the Methyl Red (MR) azo dye, are used mixed with LC and they are known as Dye Doped Liquid Crystals (DDLDC). Exposure of MR causes its molecules to undergo a brownian effect within the cell in which they migrate towards the substrates, where they are adsorbed because of electrostatic interactions at the LC-substrate interface. Afterwards, MR undergoes the same cis-trans photoisomerization process as the other azo dyes^{36,37}. Most photoalignment azo dyes absorb in the UV, which restricts their use to laboratories with specialized opti-

cal setups. By contrast, some azo dyes, like the Methyl Red, enable photoalignment in the visible range, specifically the 532 nm range, but its strong absorption leads to diattenuation effects that can compromise the performance of LC devices, thus deserving an in-depth analysis to validate this approach. In a previous paper³⁸, we have already discussed in detail the diattenuation effects on homogeneous liquid crystal cells fabricated via photoalignment. In this paper, we will extend this study into more complex devices, able to generate structured light.

Different approaches can be followed to generate the spatially variant linearly polarized light beams needed to produce complex photoaligned patterns. LCoS devices combined with a quarter-waveplate²⁷, scanning systems combined with rotating polarizers³⁷, combination of adaptive spiral phase plates³⁹ or a variable spiral plates⁴⁰ are versatile approaches. If low polarization order light is of interest, then there is no need for complicated setups with mechanically moving elements³⁷ or spatial light modulators^{41,42}. By spatially varying the polarization of the incident light using a spiral plate⁴⁰, cylindrical vector beams (CVB)⁴³ can be written onto the substrate with high precision to generate well-known q-plates^{29,30}. Devices fabricated in this way can act as geometric phase elements, modulating the light's orbital angular momentum to generate structured beams. Variations in wavelength-dependent absorption may impact the quality and efficiency of optical vortex generation, yet these effects have not been extensively studied in the literature. In this paper, as we are analyzing exclusively the visible range of the light spectrum, we will use the term "all-with-visible-light" to refer to our manufactured devices.

In this work, we address the various challenges introduced through comprehensive spectral characterisation and robust testing of absorption, achromaticity and tunability of DDLC photoaligned devices, with the objective of fully exploit the potential of visible-spectrum azo dyes in LC photonic devices. The paper is structured as follows. First, in Section II, we show the theoretical development. In Section III, we present the fabrication process and the experimental set-ups. Finally, in Section IV, we show and discuss the results obtained.

II. THEORY

As discussed in the Introduction, the azo dye employed is Methyl Red, which exhibits absorption within the visible spectrum. Consequently, the manufactured devices display diattenuation effects during operation. Therefore, we start developing a theoretical model to analyse a linear retarder with diattenuation using the Jones formalism, and afterwards we will discuss what happens when there is a spatial variation of the neutral lines when generating the well-known vortex

beams with orbital angular momentum.

A. Geometric phase and diattenuation

Throughout this work, we adopt a right-handed coordinates system to describe all vector quantities. In this system, the X and Y axes are aligned with the laboratory's horizontal and vertical directions, respectively, while the Z axis corresponds to the direction of light propagation. Right (left) handedness is defined as clockwise (counterclockwise) sense of direction from the perspective of an observer receiving the light. In general, the device can be modelled as a rotated linear retarder with diattenuation (W) as follows,

$$W(\Gamma, p_e, p_o, \theta) = R(-\theta) \cdot W_0(\Gamma, p_e, p_o) \cdot R(\theta). \quad (1)$$

, where R is the Jones rotation matrix, θ is the angle of rotation of the neutral lines, W_0 is the Jones matrix of a diattenuating retarder with its extraordinary and ordinary lines along the X and Y axes of the reference system, respectively. And p_e and p_o are the amplitude attenuation coefficients for the extraordinary and ordinary axes.

The R matrix is defined as

$$R(\theta) = \begin{pmatrix} \cos \theta & \sin \theta \\ -\sin \theta & \cos \theta \end{pmatrix}, \quad (2)$$

and the W_0 matrix can be written as

$$W_0 = \begin{pmatrix} p_e e^{-j\varphi_e} & 0 \\ 0 & p_o e^{-j\varphi_o} \end{pmatrix}, \quad (3)$$

where $e^{-j\varphi_e}$ and $e^{-j\varphi_o}$ are the phase terms related to the extraordinary and ordinary axes of the retarder. The relation between the phase terms and the retardance Γ is given by:

$$\Gamma = \varphi_e - \varphi_o = \frac{2\pi}{\lambda} d(n_e(\lambda, \alpha) - n_o(\lambda)), \quad (4)$$

where d is the thickness of the device, n_e and n_o are the extraordinary and ordinary refractive indexes respectively. n_e has a dependence with the wavelength λ and the rotation angle α of the LC molecules relative to their rest position (along the substrate plane), what is normally called tilt angle. Substituting Eq. (4) into Eq. (3) results in the following expression:

$$W_0 = e^{-j\varphi_o} e^{-j\Gamma/2} \begin{pmatrix} p_e e^{-j\Gamma/2} & 0 \\ 0 & p_o e^{j\Gamma/2} \end{pmatrix}. \quad (5)$$

Substituting Eq. (2) and (5) in Eq. (1), we obtain:

$$W(\Gamma, p_e, p_o, \theta) = e^{-j\varphi_o} e^{-j\Gamma/2} \begin{pmatrix} p_e e^{-j\Gamma/2} \cdot \cos^2 \theta + p_o e^{j\Gamma/2} \cdot \sin^2 \theta & (p_e e^{-j\Gamma/2} - p_o e^{j\Gamma/2}) \cos \theta \sin \theta \\ (p_e e^{-j\Gamma/2} - p_o e^{j\Gamma/2}) \cos \theta \sin \theta & p_e e^{-j\Gamma/2} \cdot \sin^2 \theta + p_o e^{j\Gamma/2} \cdot \cos^2 \theta \end{pmatrix}. \quad (6)$$

Applying some trigonometric identities and considering that the birefringent device is illuminated with circularly po-

larized light, as usual with PB devices, the electric field at the output can be written as follows:

$$\vec{E}_{out}(\Gamma, p_e, p_o, \theta) = \frac{e^{-j\phi_0} e^{-j\Gamma/2}}{2\sqrt{2}} \left(\begin{array}{l} (p_e e^{-j\Gamma/2} + p_o e^{j\Gamma/2}) + (p_e e^{-j\Gamma/2} - p_o e^{j\Gamma/2}) \exp(\pm j2\theta) \\ \pm j (p_e e^{-j\Gamma/2} + p_o e^{j\Gamma/2}) \mp j (p_e e^{-j\Gamma/2} - p_o e^{j\Gamma/2}) \exp(\pm j2\theta) \end{array} \right), \quad (7)$$

where in the appearances of '±' and '∓' the upper (lower) sign is related to incident light polarization right-handed circular, RHC (left-handed circular, LHC).

Very conveniently, Eq. (7) can be decomposed into the su-

perposition of a RHC and a LHC polarization state. Without any loss of generality and to ease the discussion, we will consider that the SOP for the incident light corresponds to RHC, and then the output light electric field can be expressed as,

$$\vec{E}_{out}(\Gamma, p_e, p_o, \theta) = \frac{e^{-j\phi_0} e^{-j\Gamma/2}}{2\sqrt{2}} \left\{ \begin{array}{l} (p_e e^{-j\Gamma/2} + p_o e^{j\Gamma/2}) \begin{pmatrix} 1 \\ j \end{pmatrix} + (p_e e^{-j\Gamma/2} - p_o e^{j\Gamma/2}) \exp(j2\theta) \begin{pmatrix} 1 \\ -j \end{pmatrix} \end{array} \right\}. \quad (8)$$

By rewriting the expression as a function of the average

amplitude ($p_{avg} = \frac{p_e + p_o}{2}$) and the average amplitude difference ($p_{diff} = \frac{p_e - p_o}{2}$), we can reformulate Eq. (8) as:

$$\vec{E}_{out}(\Gamma, p_e, p_o, \theta) = \frac{e^{-j\phi_0} e^{-j\Gamma/2}}{\sqrt{2}} \left\{ \begin{array}{l} [p_{avg} \cdot \cos(\Gamma/2) - j p_{diff} \cdot \sin(\Gamma/2)] \begin{pmatrix} 1 \\ j \end{pmatrix} \\ + [p_{diff} \cdot \cos(\Gamma/2) - j p_{avg} \cdot \sin(\Gamma/2)] \exp(j2\theta) \begin{pmatrix} 1 \\ -j \end{pmatrix} \end{array} \right\}. \quad (9)$$

If there is no diattenuation ($p_{avg} = 1, p_{diff} = 0$), we obtain

the more usual expression:

$$\vec{E}_{out}(\Gamma, \theta) = \frac{e^{-j\phi_0} e^{-j\Gamma/2}}{\sqrt{2}} \left\{ \begin{array}{l} \cos(\Gamma/2) \begin{pmatrix} 1 \\ j \end{pmatrix} - j \sin(\Gamma/2) \exp(j2\theta) \begin{pmatrix} 1 \\ -j \end{pmatrix} \end{array} \right\}. \quad (10)$$

Eq. (9) is central for the goals of the paper, but first it is more instructive to analyse the simplified Eq. (10). Looking at Eq. (10), the output light from the device is composed of two electromagnetic wavefronts with orthogonal circular polarizations: a first term with RHC polarized light and a second term with LHC light. These two states of polarization, despite being overlapped, are complementary, i.e. they do not interfere with each other. In the second term corresponding to the circularly polarized state complementary to the input state, there is a phase term $\exp(j2\theta)$ that does not depend on Γ , but on the device's relative orientation of its neutral lines. This term is known as the geometric phase, which, unlike the dynamic phase, does not depend on the optical path travelled and the wavelength λ , thus it has an achromatic character, which is important for the goals of this work.

The retardance Γ in Eq. (10) can be adjusted, so that one of the two terms cancels, what makes possible to choose between the first, constant, term and the second term with the geometric phase associated. For the case when Γ is 180° (half-wave plate) or an odd multiple: $(2n + 1) \cdot 180^\circ$ with n an integer, only the geometric phase is produced:

$$\vec{E}_{out}(\pi, \theta) = \frac{e^{-j\phi_0}}{\sqrt{2}} \exp(j2\theta) \begin{pmatrix} 1 \\ -j \end{pmatrix}. \quad (11)$$

Returning to Eq. (9), the diattenuation does affect the output beam, but the geometric phase term $\exp(j2\theta)$ itself is unaffected. However, despite the geometric phase's independence, even with $\Gamma = 180^\circ$, the first term associated to the right-handed circularly polarized light does not disappear: so

in contrast with the previous discussion for Eq. (10), now the output beam would be a combination of the two terms of different polarization. We cannot cancel any of the overlapped terms, but we can choose a Γ that makes minimum the intensity of one of the orthogonal polarizations, as we will demonstrate in Section IV. The complementary term would contain the geometric phase while the other term would be superimposed light that will reduce the contrast of the image obtained. However, depending on the design for the spatial variations of the angle θ , they do not need to spatially overlap at the plane of interest for the application, as we explain in the last paragraph in the next Subsection.

B. Spatially variant neutral lines devices

The dependence of the geometric phase on the spatially dependent orientation of the neutral lines allows the creation of different phase elements. In order to analyse this behaviour, we express the coordinates of the device plane in a polar reference system, where r and φ are the radial and azimuthal coordinates, respectively. In the present paper, we are mainly interested in two equivalent situations, which are the ones that can be produced by the VSP:

a. $\theta(r, \varphi) = \varphi$. The illuminating wavefront generated through the VSP is azimuthally polarized. The neutral lines orientation generated on the DDLC device through photoalignment points along the radius from the centre of the device. The geometric phase term in the Eqs. in the previous Subsection can be written as $f(\theta = \varphi) = \exp(j2\varphi)$, which is equivalent to a beam with orbital angular momentum of topological charge of 2.

b. $\theta(r, \varphi) = \varphi + \frac{\pi}{2}$. The VSP generates radially polarized light. The neutral lines generated on the DDLC device points azimuthally and concentrically around the centre of the device, implying that the geometric phase term is written as $f(\theta = \varphi + \frac{\pi}{2}) = \exp(j(2\varphi + \pi))$. Again, this implies that the output beam has a topological charge of 2, but 180° out of phase compared to case *a*.

To sum it up, we will produce q-plates able to generate vortex beams with topological charge 2. In Fig. 1, we show a graphical representation of the overlapped wavefronts when considering Eq. (9) and (10): we have the optical vortex associated with the term with the geometric phase, and the planar wavefront associated with the other term of the equation. Since the two wavefronts have complementary circular polarization states, we could filter one of them by a convenient arrangement of a quarter-wave plate and a linear polarizer. In this case, at least 50% of the energy is lost. In general, what is done is to produce the needed retardance $\Gamma = 180^\circ$ (or odd multiples) so that the vortex beam is generated with maximum efficiency. Resulting from Eq. (9), in the presence of diattenuation, even for $\Gamma = 180^\circ$ (or odd multiples), there is an overlap with the planar wavefront given by the orthogonal polarization term. This spatial overlap, however, disappears in the far-field, usually the regime of observation of vortex beams in applications, where the helical wavefront generates an intensity ring and the planar wavefront corresponds to light in the center,

thus not affecting the helical phase along the ring.

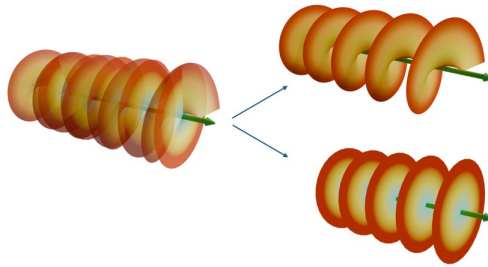


FIG. 1. Output beam from the photoaligned device, where two different wavefronts overlap each other: a planar wavefront and a helical wavefront, each of them associated to the two orthogonal circularly polarized states. If the input beam has RHC polarization, then the optical vortex will have LHC polarization, and the planar wavefront RHC polarization.

III. SAMPLE PREPARATION AND EXPERIMENTAL SETUP

Liquid crystal devices incorporating Methyl Red doped LC layers were fabricated via photoalignment technique. The substrates employed consisted of $25 \text{ mm} \times 37.5 \text{ mm}$ glass slides coated with a 23 nm layer of Indium Tin Oxide (ITO). As a first step, the substrates underwent a surface treatment, which included a cleaning process with acetone (Merck, Darmstadt, Germany) and an ultrasonic bath for a duration of 15 minutes (Equipos Clínicos, Jaen, Spain), followed by drying in an oven (Fisher Scientific, Madrid, Spain) at 120°C for 20 minutes. Subsequently, the surface was exposed to UV ozone treatment for 15 minutes using an Ossila UV Ozone Cleaner (Ossila, Sheffield, UK). The cells were then assembled using two substrates and silica spacers ($5.5 \mu\text{m}$, Whitehouse Scientific, Chester, UK) to define the thickness of the devices. The selected thickness value ensured that retardances exceeding 2π could be obtained. The spacers were deposited via spin-coating, and two sides of the cell were sealed with a UV adhesive (Norland Optical Adhesive 61, Edmund Optics, Barrington, USA)³⁸.

A liquid crystal mixture containing 99 wt% E7 (Nematel, Mainz, Germany) and 1 wt% Methyl Red MR (Merck, Darmstadt, Germany) was introduced into the cells through capillary action. To optimize filling and ensure uniform distribution of the LC, the process was conducted at approximately 65°C , which is the temperature of the isotropic phase of the LC, where the molecules lose its birefringence, and it behaves like a liquid. This isotropic condition allows for the simultaneous photoalignment of both cell surfaces, using a method known as double-sided photoalignment⁴⁴. The thickness of our device was measured using a known interferometric method that we recently used in our last work³⁸, obtaining a value of $7.4 \mu\text{m}$.

The photoalignment set-up is shown in Fig. 2. First, a 532 nm laser beam (Verdi-V5, Coherent, Copenhagen, Denmark) is expanded and collimated by a combination of spatial filter

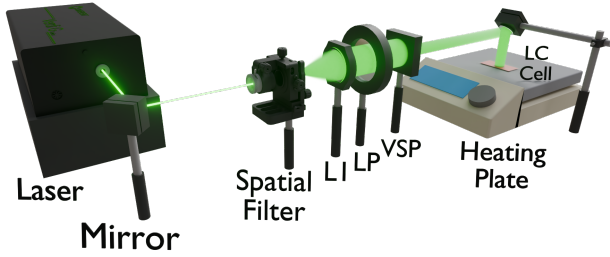


FIG. 2. Photoalignment setup.

and a lens (L1). Then, we obtain linearly polarized light along the vertical axis of the laboratory through a linear polarizer (LP), which passes through the Variable Spiral Plate (VSP, ArcOptix, Neuchatel, Switzerland)⁴⁰, capable of generating structured light: specifically radial and azimuthally polarized light. Finally, this structured polarized light impinges perpendicular to the LC cell, which is at a temperature of 65 °C in order to keep it in an isotropic state to ensure a correct photoalignment in both areas of the substrates. The photoaligned area of our devices is 1 cm in diameter, since that is the size of the aperture of the VSP. With this assembly, we can generate photoaligned devices with an azimuthal (and/or radial) distribution of the LC molecules.

Fig. 3 shows the set-up for the characterisation of the manufactured devices. In this case, the cell was illuminated by a supercontinuum laser (NKT Compact, NKT Photonics, Birkerod, Denmark) with a wavelength selector (SuperK Varia, NKT Photonics, Birkerod, Denmark). The laser was operating at its maximum spectral bandwidth (450 – 850 nm) covering all the visible spectrum. First, the beam is collimated with a combination of a spatial filter and a lens L1 (focal = 70 mm) and its diameter is adjusted with the diaphragm (D) to determine the area to be analysed (around 0.8 cm²). As established in Section II, to produce the vortex beam, we have to illuminate the device with circularly polarized light. For that we use a combination of a linear polarizer (LP) with its transmission axis positioned at 0° and a quarter-wave plate retarder with its neutral lines oriented at 45° to the laboratory's horizontal. Finally, at the focal plane of lens L2 (focal = 200 mm), we are able to obtain the far field pattern of the beam. To capture the optical vortices at the lens focal plane, a microscope objective is used, allowing an image of adequate size to be captured by the camera sensor (CS126CU CMOS colour Camera, Thorlabs, New Jersey, USA).

Once the setup has been established, before showing the experimental results, we can theoretically simulate the optical vortices that we should obtain in the focal plane of L2. Knowing that the focal length is 200 mm and the illuminated area of the photoaligned q-plate is 0.8 cm² approximately, we can simulate the behaviour of the device for the three wavelengths we will study along the paper: 473 nm, 532 nm and 633 nm. In Fig. 4, in subfigure (a), we can see the phase profile of the helical wavefront at the exit of the DDLC cell, which corresponds to a geometric phase with a topological charge of 2 when RHC light is incident. Subfigures (b-d), show the theo-

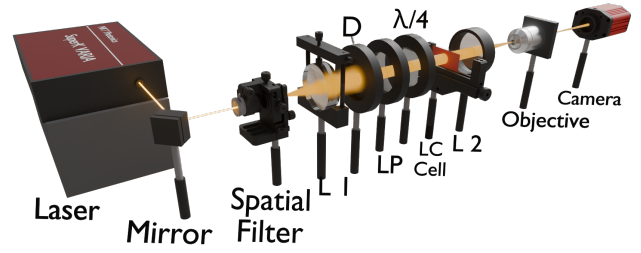


FIG. 3. Characterization setup.

retical optical vortices that we should obtain at the focal plane of L2 with lengths expressed in laboratory coordinates for the sake of comparison with the experimental images in the next Section. As we can observe, its diameter increases slightly with the wavelength, and the ring diameter is about 20 μm diameter.

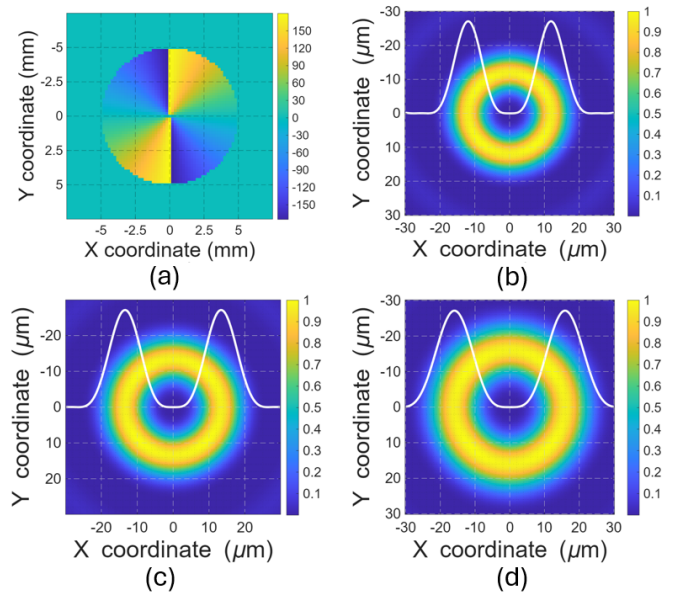


FIG. 4. Laboratory scaled simulation of the optical vortices generated by our photoaligned q-plate, where (a) shows the phase profile generated by a q-plate with topological charge 2 and (b-d) are the optical vortices obtained when the incident wavelength is 473 nm, 532 nm and 633 nm, respectively, at the focal plane of lens L2.

It is important to note that our experimental setup introduces a certain degree of tolerance, particularly in the positioning of the magnifying objective at the focal plane of L2. As a result, slight discrepancies between the size of the optical vortices are to be expected between the experimental results and the simulated ones.

IV. RESULTS

Since the results obtained from the radially and azimuthally photoaligned devices are similar, in this Section we will only analyse the azimuthal patterns, as we found that it is the most

efficient configuration with the current materials and VSP setup available in our laboratory. The study of the device was carried out in terms of voltage response and wavelength-dependent behaviour, with a focus on the voltage values that make this behaviour independent of the wavelength across the visible spectrum (achromaticity).

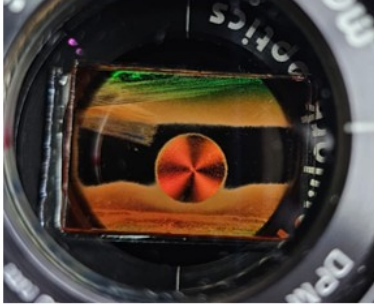


FIG. 5. q-plate of 7.4 μm thickness between crossed polarizers.

In Fig. 5, we show the pattern of a device azimuthally photoaligned, when placed between two crossed polarizers and ambient illumination. It can be appreciated with great definition the circular aperture of the photoalignment process, where we can clearly see the four orthogonal nulls of intensity, what implies a good photoalignment quality.

Let us first provide an estimation of the magnitude of the planar wavefront which is added to the vortex beam when there is diattenuation. For that, we have to check the optimal value of Γ so that we obtain maximum intensity I_{max} for the geometric phase term and minimum intensity I_{min} for the first term. From Eq. (9), the intensity associated with each term can be calculated as:

$$I_1 = \left| \left(\frac{p_e + p_o}{2} \right) \cos(\Gamma/2) - j \left(\frac{p_e - p_o}{2} \right) \sin(\Gamma/2) \right|^2 \quad (12)$$

$$I_2 = \left| \left(\frac{p_e - p_o}{2} \right) \cos(\Gamma/2) - j \left(\frac{p_e + p_o}{2} \right) \sin(\Gamma/2) \right|^2, \quad (13)$$

where I_1 and I_2 are the intensities associated with the first and second terms of Eq (9), respectively.

After some manipulations and simplifying these expressions with the use of trigonometric identities, we obtain:

$$I_1 = \frac{1}{4} (p_e^2 + p_o^2 + 2p_e p_o \cos \Gamma) \quad (14)$$

$$I_2 = \frac{1}{4} (p_e^2 + p_o^2 - 2p_e p_o \cos \Gamma). \quad (15)$$

It is easy to notice that the term that minimizes Eq. (14) and maximizes Eq. (15) is $\Gamma = (2n + 1) \cdot 180^\circ$, with n an integer.

$$I_{1,min} = \frac{1}{4} (p_e - p_o)^2 \quad (16)$$

$$I_{2,max} = \frac{1}{4} (p_e + p_o)^2. \quad (17)$$

So, if we consider Eq. (9) for odd multiples of 180° and for a q-plate with azimuthal orientation of the neutral lines illuminated with RHC polarized light, the output wavefront is:

$$\vec{E}(180^\circ, \varphi) = \frac{e^{-j\varphi_0}}{2\sqrt{2}} \left[p_{diff} \begin{pmatrix} 1 \\ j \end{pmatrix} + p_{avg} e^{j2\varphi} \begin{pmatrix} 1 \\ -j \end{pmatrix} \right]. \quad (18)$$

We see that the quotient of both intensities in Eq. (16) and (17) gives the relative weight of the planar wavefront:

$$R_{opt} = \left(\frac{p_e - p_o}{p_e + p_o} \right)^2. \quad (19)$$

Using the amplitude absorption coefficients we measured in our last work³⁸ for a device of 8.4 μm thickness (see Table 2 in Moya et al.³⁸) and applying Eq. (19), we obtain the corresponding values in Table I for R_{opt} . Note that these values are comparable with the 7.4 μm device because the thickness difference is small, so the absorption values will be similar.

Therefore, with Table I, we show that diattenuation effects might have a very small influence on the quality of the vortex beams generated with the "all-with-visible-light" approach. In particular, we confirm that at longer wavelengths, red part of the spectrum, where no diattenuation exists, the value for R_{opt} is almost zero. Diattenuation increases as wavelength decreases. However, even in the blue part of the spectrum, at 473 nm, we see that R_{opt} is still very small, close to 1%. In the next subsections we proceed with a more detailed analysis of the tunability and achromaticity achievable with the DDLC fabricated device.

TABLE I. Absorption coefficients from Moya et al.³⁸ and the intensity ratio R_{opt} between planar wavefront and vortex beam, where p_e and p_o correspond to p_x and p_y used in that paper, respectively.

λ (nm)	p_e	p_o	R_{opt} (%)
473	0.62	0.79	1.45
532	0.70	0.84	0.83
633	0.87	0.91	0.05

A. Tunability

As discussed in Section II, the state where the geometric phase of the device generates more efficiently an optical vortex is reached when Γ is an odd multiple of 180° . Experimentally, to obtain an optical vortex using the device, it is necessary to apply a certain voltage to the sample, in order to reach this Γ value. A voltage sweep is performed to determine all the 180° phase shift multiples produced by the device.

During this process, the appearance of a well-defined optical vortex ring indicates that a retardance close to 180° has been achieved. In practice, there is a tolerance range and it is not necessary to have a Γ value of exactly 180° : the optical vortex will appear with a good contrast within a voltage interval.

Furthermore, to evaluate the tunability of the device across the visible spectrum, three primary wavelengths were chosen to have a proper sampling: red (633 nm), green (532 nm) and blue (473 nm). They correspond as well to laser wavelengths typically found in many laboratories.

For the results, we have selected two optical vortices with the best contrast, because in the case of light of 532 nm and 473 nm, our device was able to generate a total of three and four optical vortices, but with very short voltage intervals. We note that the two more robust vortices appeared at the larger voltages. In the case of the 633 nm wavelength, two optical vortices were achievable. In Table II, we show these results for the two voltage intervals studied. We note that voltages are below 5 V in any case. The threshold voltage, when the molecules of LC E7 in our devices start to be affected by the electric field, is around 1 V.

In Fig. 6, we present the intensity distributions of our device under the three different wavelengths. With a horizontal cut across the centre, we can appreciate the profile in the light distribution. The actual size of the patterns of the focal plane of lens L2 can be deduced from the $10\ \mu\text{m}$ scale bar included in the image (a) and they are consistent with the sizes provided in the simulated images in Fig. 4.

TABLE II. Tunability: Voltage intervals where the vortex beam shows the best contrast for each of the three RGB wavelengths. ΔV_1 and ΔV_2 correspond to the occurrences at the two larger voltages (described in the text).

λ (nm)	ΔV_1 (V)	ΔV_2 (V)
473	1.7-1.8	3.4-4.1
532	1.5-1.7	2.9-3.6
633	1.3-1.5	2.4-3.1

As shown in Fig. 6, each row represents a different state of the total wavefront generated by our device. As we have analysed in Eq. (9), depending on the retardance Γ and, therefore, the applied voltage, we will have different combinations where the planar and helical wavefronts will have different weights. In the first row (Fig. 6 (a-c)), we apply a voltage of 0 V, which means that we are not manipulating the weight of each term, and depending on the thickness and wavelength, we will have different situations. For example, at 532 nm, there is no optical vortex, and the dominant term of Eq. (9) is the first, corresponding to the planar wavefront. On the other hand, for 473 nm and 633 nm, we can see that there is a combination of both terms, so both wavefronts are overlapped. Looking at the intensity profile, we can deduce that in the case of 633 nm, the two terms have similar weights, while for 473 nm, the planar wavefront term is larger. Next, we modified the voltage, trying to achieve situations where one of the terms dominates over the other. In the second row (Fig. 6 (d-f)), we show the first of the optical vortices described in Table II. In

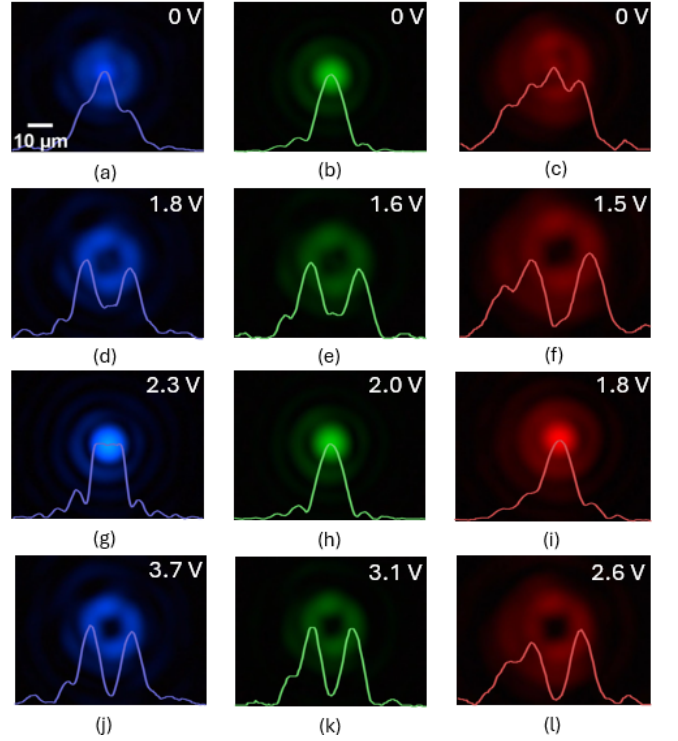


FIG. 6. Intensity distributions together with horizontal cut across the centre of the cell for 473 nm, 532 nm and 633 nm, respectively at the first, second and third columns. In each subfigure, we show the applied voltages related to off-state (first row), second-to-last vortex (second row), intermediate planar wavefront (third row) and last vortex (fourth row).

this case, the optical vortex can be clearly observed. It is interesting to notice the better contrast obtained for 633 nm with respect to the 532 nm and 473 nm cases. This is probably due to the absence of diattenuation at 633 nm, as shown in Table I. Therefore, the residual planar wavefront in Eq. (18), given by the weight of p_{diff} , is totally cancelled. In the third row (Fig. 6 (g-i)), we have a state where the planar wavefront dominates. And finally, in the fourth row (Fig. 6 (j-l)), we present the second optical vortex, corresponding to the wider voltage ranges presented in Table II. It is interesting to note that in this case, the contrast is very good for all three wavelengths. These results agree with the theoretical results described in Table I, since the effects of diattenuation affect at most 1.45% in the case of blue light (473 nm). In addition, the sizes of the optical vortices and the increase in diameter with larger wavelengths are consistent with those obtained in the simulation in Fig. 4, which validates our experimental methodology to manufacture this type of devices.

From a theoretical point of view, we can justify that the voltages required to reach the 180° phase shift odd multiples decrease as the wavelength increases (as happens at each of the rows in Fig. 6), analysing the relationship between the physical variables in the retardance equation, described by Eq. (4). The specific values of the extraordinary and ordinary refractive indices for E7 (the LC used in this work) can be obtained from Moya et al³⁸, and more generally from Li et al⁴⁵.

Looking at Eq. (4), Γ is inversely proportional to the wavelength λ and proportional to the thickness d and the difference between the refractive indices (Δn), the latter depending on the voltage. In parallel aligned devices, the maximum value for Δn , thus also for Γ , occurs at 0 Volts and then decreases with the increase in the voltage. Therefore, for a device of thickness d and considering a retardance value Γ , we need to decrease the voltage as the wavelength increases. This justifies the results shown in Table II, where the voltage values for the device are smaller when characterised using light of 633 nm.

With Eq. (4), we can also predict the number of optical vortices we can obtain depending on the wavelength λ used. In the 2-dimensional colour plot in Fig. 7, the retardance values Γ are shown as a function of the visible wavelengths (Y-axis) and the tilt angles (X-axis). Note that in parallel aligned LC devices, as our DDLC cell, the tilt angle increases (non-linearly) with the increase in the applied voltage³⁸. We can also appreciate the white lines that correspond to the values of Γ equal to $(2n + 1) \cdot 180^\circ$. Horizontal lines are overlapped for the 3 wavelengths analysed in this work (473/532/633 nm). Also, vertical lines at tilt voltages 10° and 45° are indicated, which will be used in the next Subsection. Following these theoretical results, for our device of $7.4 \mu\text{m}$, we should obtain two optical vortices for 633 nm, three for 532 nm and four for 473 nm, which agrees with the experimental results, discussed when introducing Table II and shown in Fig. 7. In addition, with this figure, we can appreciate the approximate theoretical retardance ranges of the device: 5π for 633 nm, 7π for 532 nm and 8π for 473 nm. By analogy with our experimental results and the voltage ranges used, we can deduce that the last optical vortex shown in Fig. 6 (fourth row) for each wavelength corresponds to a retardance Γ of 180° (first white line from the right) and the other one appearing at a lower voltage (second row in Fig. 6) to Γ equal to 540° approximately (second white line from the right in Fig. 7). In Fig. 7, we can also appreciate more clearly the effect we have just discussed about the dependence of Γ with the tilt angle (voltage) and the wavelength: so for a fix value of retardance, the tilt angle decreases when the wavelength increases.

As we have already explained, Γ has a dependence on the wavelength λ and the tilt angle α (angle between the long axis of the LC molecule and the plane of the substrate), so we can study the evolution of the retardance as a function of λ or α . In Fig. 8 we can see the relationship between the tilt angle related dispersion $\left(\left| \Gamma'_\alpha \right| = \left| \frac{\partial \Gamma}{\partial \alpha} \right| \right)$ and the tilt angle. This figure describes how fast the retardance changes for three different wavelengths along the tilt angles, i.e. as a function of the applied voltage. As the tilt angle increases, the rate of change in the dispersion becomes progressively slower, which explains why the variation in retardance decreases at higher voltages and why the second singularity can be observed over a larger range of voltages, as we obtained in the results from Table II and Fig. 6. So, from these results and from the tunability point of view, we can assume that the optical vortices obtained with a retardance of 180° are preferable, because they are more stable (wider voltage range) and show a better contrast. Note that in Fig. 8, the profile for each wavelength is basically the same

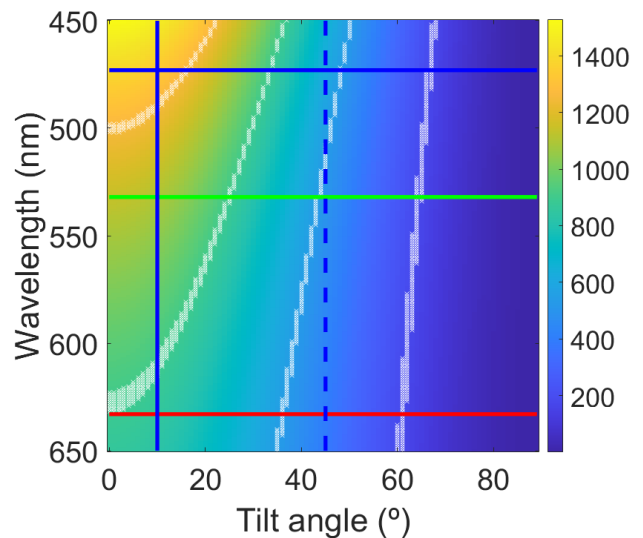


FIG. 7. Colour plot of the retardance vs tilt angle for the visible spectrum for the $7.4 \mu\text{m}$ cell fabricated in the paper. The horizontal lines marks the three primary wavelengths studied (473 nm, 532 nm and 633 nm), while the vertical lines marks the two tilt angles (10° and 45°) studied in the Achromaticity Subsection.

apart from a constant scale factor; with values of 0.36 and 0.64 for 633 nm and 532 nm when calculated with respect to the dispersion at 473 nm.

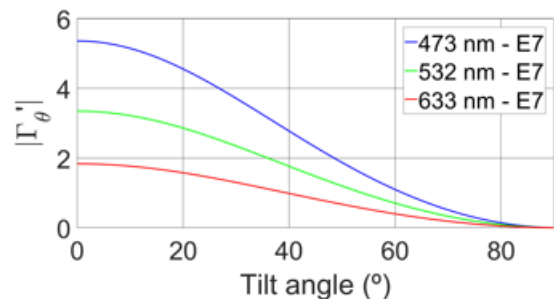


FIG. 8. Tilt angle dispersion of the retardance Γ as a function of the tilt angle of LC molecules for $7.4 \mu\text{m}$.

B. Achromaticity

For the study of the achromaticity of the device, various sweeps will be performed for the three wavelengths considered. Before presenting the results, it is important to define the characterization criteria employed in this study. The images were captured using a 12-bit depth camera, allowing measurements across 4096 greyscale levels, where 0 corresponds to absolute black and 4096 to pure white. Based on this, any greyscale value exceeding 1024 in the singularity area will be considered as a deviation from black, and thus, the optical vortex will no longer be regarded as exhibiting a true singularity. Obviously, a lower greyscale value could also be chosen.

However, with the threshold of 1024 we observe that the centre is still very dark, thus it is a reasonable criteria.

In the first set of measurements, for each of the three wavelengths (473, 532 and 633 nm), the voltage is fixed at the value for which the optical vortex exhibits the maximum contrast. These voltages correspond to the middle value shown in Table II for ΔV_2 at each of the wavelengths. Subsequently, the spectral bandwidth is gradually increased in order to evaluate the spectral response of the device. Table III presents the assigned voltage together with the wavelength ranges over which the singularity continues to meet the previously defined criterion. Additionally, Fig. 9 shows the optical vortices related to the maximum spectral bandwidths $\Delta\lambda$ indicated in Table III, and for each of the three wavelengths. We can appreciate that the three vortices show a good contrast with a dark center, specially for 633 nm.

TABLE III. Achromaticity: Spectral bandwidths within which the optical vortex singularity shows a good contrast at each of the three wavelengths.

λ (nm)	Voltage (V)	$\Delta\lambda$ (nm)
473	3.7	65
532	3.1	90
633	2.6	100

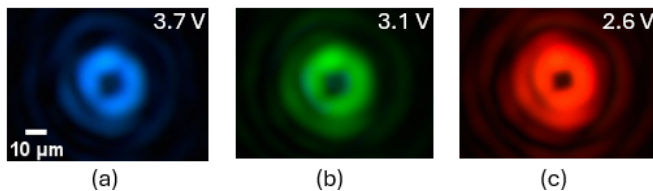


FIG. 9. Optical vortices centered at 473, 532 and 633 nm wavelength, with the illumination spectral bandwidth of (a) 65 nm, (b) 90 nm and (c) 100 nm (as shown in Table III).

Our results are supported by theoretical calculations, where in Fig. 10, the relationship between the chromatic dispersion of the retardance $\left(|\Gamma'_\lambda| = \left|\frac{\partial\Gamma}{\partial\lambda}\right|\right)$ with the wavelengths is shown for two tilt angles. In this figure, we can clearly see how the chromatic dispersion is lower for higher values of λ and higher tilt angles (voltages), justifying that the best achromatic behaviour corresponds to the situation where the device is applied larger voltages and illuminated by light at 633 nm, as demonstrated experimentally in Table III. It is also interesting to notice that the two curves for different tilt angles have almost the same profile apart from a scale factor of 2.15.

We see that the wide wavelength ranges validate the usage of the q-plates not only with laser light but also with broad-band illumination from, for example, LED light sources.

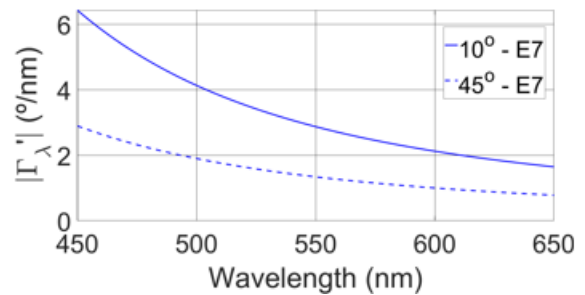


FIG. 10. Chromatic dispersion of the retardance Γ as a function of the tilt angle of LC molecules.

V. CONCLUSIONS

This work demonstrates the successful fabrication of devices photoaligned with visible light (532 nm) based on MR doped LC, capable of generating optical vortices through a simple photoalignment setup, which employs a commercially available Variable Spiral Plate to induce radial or azimuthal alignment patterns.

The optical performance of the devices was thoroughly characterized across the entire visible spectrum, including wavelengths where the azo dye MR shows strong absorption and diattenuation. Remarkably, the device was able to produce structured light even in these, a priori, non-favourable spectral areas, indicating that such absorption does not prevent practical functionality. Novel analytical expressions were developed highlighting the role of diattenuation in geometric phase-based devices, and enabling to quantify its effect through the R_{opt} magnitude.

Furthermore, the device's characterization was evaluated in terms of tunability and achromaticity, demonstrating reliable and consistent performance, which validated the proposed fabrication method's versatility and reliability. Both, experimentally and theoretically, we have shown that, in case of various achievable 180° retardance odd multiples, better results in terms of voltage tunability robustness and achromaticity are produced for the one produced at a larger voltage. The effects of diattenuation do not greatly affect the performance of these "all-with-visible-light" devices, where the worst case scenario is with 473 nm, where the contrast is reduced by 1.45% (R_{opt} magnitude), which is a small degradation of the contrast. These findings provide valuable insight into the design of ultrathin geometric phase optical elements for the generation of structured light using photoalignment.

VI. ACKNOWLEDGEMENTS

This work was supported by the Grant CIPROM/2024/90 funded by Generalitat Valenciana (Spain), Grant PID2023-148881OB-I00 funded by MICIU/AEI/10.13039/501100011033 and by "ERDF/EU" (Spain) and Grant PID2024-161610OB-I00 funded by MICIU/AEI/10.13039/501100011033 and by "ERDF/EU". ARS-M

is grateful to the “Generalitat Valenciana” for the grant (GRISOLIAP/2021/106).

VII. AUTHOR DECLARATIONS

A. Conflict of Interest

The authors have no conflicts to disclose.

B. Author Contributions

Adrián Moya: Conceptualization (equal); Data curation (equal); Formal analysis (equal); Investigation (equal); Methodology (equal); Software (equal); Validation (equal); Visualization (equal); Writing-original draft (equal). **Adriana R. Sánchez-Montes:** Methodology (equal); Software (equal). **Sergi Gallego:** Funding acquisition (equal); Resources (equal); Writing-review & editing. **Eva M. Calzado:** Conceptualization (equal); Methodology (equal); Project administration (equal); Resources (equal); Supervision (equal); Writing-review & editing (equal). **Andrés Márquez:** Conceptualization (equal); Formal Analysis (equal); Funding acquisition (equal); Methodology (equal); Project administration (equal); Resources (equal); Software (equal); Supervision (equal); Visualization (equal); Writing-review & editing (equal). **Inmaculada Pascual:** Funding acquisition (equal); Writing-review & editing (equal). **Augusto Beléndez:** Funding acquisition (equal); Resources (equal).

VIII. DATA AVAILABILITY

The data that supports the findings of this study are available from the corresponding author upon reasonable request.

IX. REFERENCES

- ¹O. Yaroshchuk and Y. Reznikov, “Photoalignment of liquid crystals: basics and current trends,” *J. Mater. Chem.* **22**, 286–300 (2012).
- ²X. Xi, C. Yan, L. Z. Shen, Y. Wang, and P. Cheng, “Liquid crystal photoalignment technique: Basics, developments, and flexible/stretchable device applications,” *Materials Today Electronics* **6**, 100069 (2023).
- ³V. G. Chigrinov, V. M. Kozenkov, and H. Kwok, *Photoalignment of Liquid Crystalline Materials* (Wiley, 2008).
- ⁴J. Stöhr and M. Samant, “Liquid crystal alignment by rubbed polymer surfaces: a microscopic bond orientation model,” *Journal of Electron Spectroscopy and Related Phenomena* **98-99**, 189–207 (1999).
- ⁵Y. Cui, R. S. Zola, Y.-C. Yang, and D.-K. Yang, “Alignment layers with variable anchoring strengths from polyvinyl alcohol,” *Journal of Applied Physics* **111** (2012), 10.1063/1.3697680.
- ⁶J. Prakash, A. Kumar, and S. Chauhan, “Aligning liquid crystal materials through nanoparticles: A review of recent progress,” *Liquids* **2**, 50–71 (2022).
- ⁷H. Xin, H. Chen, P. Song, and Q. Sun, “Alignment control of thermotropic liquid crystals by topography and chemical functionality of a surface: A review,” *Materials Today Communications* **36**, 106680 (2023).
- ⁸D.-R. Chiou, L.-J. Chen, and C.-D. Lee, “Pretilt angle of liquid crystals and liquid-crystal alignment on microgrooved polyimide surfaces fabricated by soft embossing method,” *Langmuir* **22**, 9403–9408 (2006).
- ⁹A. Muravsky and A. Murauski, “Q&a of liquid crystal alignment: theory and practice,” *Frontiers in Soft Matter* **4** (2024), 10.3389/frsfm.2024.1382925.
- ¹⁰V. Chigrinov, J. Sun, and X. Wang, “Photoaligning and photopatterning: New lc technology,” *Crystals* **10**, 323 (2020).
- ¹¹I. Nys, B. Berteloot, and K. Neyts, “Photoaligned liquid crystal devices with switchable hexagonal diffraction patterns,” *Materials* **15**, 2453 (2022).
- ¹²A. Muravsky, A. Murauski, X. Li, V. Chigrinov, and H. Kwok, “Optical rewritable liquid-crystal-alignment technology,” *Journal of the Society for Information Display* **15**, 267–273 (2007).
- ¹³W. Duan, P. Chen, B.-Y. Wei, S.-J. Ge, X. Liang, W. Hu, and Y.-Q. Lu, “Fast-response and high-efficiency optical switch based on dual-frequency liquid crystal polarization grating,” *Optical Materials Express* **6**, 597 (2016).
- ¹⁴J. Sun, A. K. Srivastava, L. Wang, V. G. Chigrinov, and H. S. Kwok, “Optically tunable and rewritable diffraction grating with photoaligned liquid crystals,” *Optics Letters* **38**, 2342 (2013).
- ¹⁵Y.-H. Huang, S.-W. Ko, S.-C. Chu, and A. Y.-G. Fuh, “High-efficiency fresnel lens fabricated by axially symmetric photoalignment method,” *Applied Optics* **51**, 7739 (2012).
- ¹⁶A. Forbes, M. de Oliveira, and M. R. Dennis, “Structured light,” *Nature Photonics* **15**, 253–262 (2021).
- ¹⁷C. Rosales-Guzmán and V. Rodríguez-Fajardo, “A perspective on structured light’s applications,” *Applied Physics Letters* **125** (2024), 10.1063/5.0236477.
- ¹⁸C. Li, T. Wieduwilt, F. J. Wendisch, A. Márquez, L. de S. Menezes, S. A. Maier, M. A. Schmidt, and H. Ren, “Metafiber transforming arbitrarily structured light,” *Nature Communications* **14**, 7222 (2023).
- ¹⁹M. A. A. Neil, R. Juškaitis, and T. Wilson, “Method of obtaining optical sectioning by using structured light in a conventional microscope,” *Optics Letters* **22**, 1905 (1997).
- ²⁰S. Dong, P. Nanda, K. Guo, J. Liao, and G. Zheng, “Incoherent fourier ptychographic photography using structured light,” *Photonics Research* **3**, 19 (2015).
- ²¹L. Gao, L. Xu, W. Wang, X. Liu, Y. Cai, and Y. Wan, “Exploring the potential of random lasers for vortex beam generation and image edge enhancements,” *APL Photonics* **10** (2025), 10.1063/5.0284235.
- ²²Y. Yang, Y.-X. Ren, M. Chen, Y. Arita, and C. Rosales-Guzmán, “Optical trapping with structured light: a review,” *Advanced Photonics* **3** (2021), 10.1117/1.AP.3.3.034001.
- ²³A. Kritzinger, A. Forbes, and P. B. C. Forbes, “Optical trapping and fluorescence control with vectorial structured light,” *Scientific Reports* **12**, 17690 (2022).
- ²⁴A. Trichili, C. Rosales-Guzmán, A. Dudley, B. Ndagano, A. B. Salem, M. Zghal, and A. Forbes, “Optical communication beyond orbital angular momentum,” *Scientific Reports* **6**, 27674 (2016).
- ²⁵A. Belmonte, C. Rosales-Guzmán, and J. P. Torres, “Measurement of flow vorticity with helical beams of light,” *Optica* **2**, 1002 (2015).
- ²⁶J. Tian, L. Min, Y. Chen, L. Jing, P. Yang, K. Zeng, L. Zeng, Y. Ke, and X. Zhou, “Reconfigurable generation and spin manipulation of structured beams based on cascaded liquid crystal pancharatnam–berry phase elements,” *Laser & Photonics Reviews* **19** (2025), 10.1002/lpor.202401378.
- ²⁷Y. Li, Y. Liu, S. Li, P. Zhou, T. Zhan, Q. Chen, Y. Su, and S.-T. Wu, “Single-exposure fabrication of tunable pancharatnam–berry devices using a dye-doped liquid crystal,” *Optics Express* **27**, 9054 (2019).
- ²⁸M. Beijersbergen, R. Coerwinkel, M. Kristensen, and J. Woerdman, “Helical-wavefront laser beams produced with a spiral phaseplate,” *Optics Communications* **112**, 321–327 (1994).
- ²⁹A. Sit, F. D. Colandrea, A. D’Errico, and E. Karimi, “Spatially twisted liquid-crystal devices,” *APL Photonics* **9** (2024), 10.1063/5.0191411.
- ³⁰A. Rubano, F. Cardano, B. Piccirillo, and L. Marrucci, “Q-plate technology: a progress review [invited],” *Journal of the Optical Society of America B* **36**, D70 (2019).
- ³¹R. Grunwald, M. Jurke, M. Bock, M. Liebmann, B. P. Bruno, H. Gowda, and U. Wallrabe, “High-flexibility control of structured light with combined adaptive optical systems,” *Photonics* **9**, 42 (2022).

- ³²A. R. Sánchez-Montes, A. Moya, E. M. Calzado, F. J. Martínez-Guardiola, A. Márquez, J. Francés, I. Pascual, and A. Beléndez, “Two-dimensional full-stokes characterization of parallel-aligned liquid crystal on silicon spatial light modulators,” *Results in Physics* **77**, 108429 (2025).
- ³³A. R. Sánchez-Montes, A. Moya, E. M. Calzado, F. J. Martínez-Guardiola, A. Márquez, J. Francés, I. Pascual, and A. Beléndez, “Full control of arbitrary linearly polarized structured light wavefronts using PA-LCoS devices,” [Manuscript submitted for publication] (2025).
- ³⁴C.-K. Liu, S.-H. Liao, C.-T. Huang, and K.-T. Cheng, “Fabrication of azimuthally/radially symmetric liquid crystal plates using two-step photoalignments,” *Optics Express* **31**, 21962 (2023).
- ³⁵S.-W. Ko, Y.-Y. Tzeng, C.-L. Ting, A. Y.-G. Fuh, and T.-H. Lin, “Axially symmetric liquid crystal devices based on double-side photo-alignment,” *Optics Express* **16**, 19643 (2008).
- ³⁶C.-Y. Huang, Y.-R. Lin, K.-Y. Lo, and C.-R. Lee, “Dynamics of photoalignment in azo-dye-doped liquid crystals,” *Applied Physics Letters* **93** (2008), 10.1063/1.3021379.
- ³⁷A. Y.-G. Fuh, T.-H. Lin, Y.-Y. Chen, C.-C. Li, and H.-C. Jau, “Optical control of the rotation of cholesteric liquid crystal gratings,” *Optics Express* **27**, 10806 (2019).
- ³⁸A. Moya, A. R. Sánchez-Montes, E. J. Mena, M. Ortuño, M. L. Álvarez, E. M. Calzado, and A. Márquez, “Polarimetric-based analysis and manufacturing of dye-doped liquid crystal photoaligned cells for the visible range,” *Polymers* **17**, 2489 (2025).
- ³⁹M. del Mar Sánchez-López, A. Walewska, N. Bennis, J. F. Algorri, P. Sobotka, M. Zyczkowski, and I. Moreno, “Liquid-crystal adaptive equivalent q-plate device with tunable topological charge,” *Optics Express* **33**, 20573 (2025).
- ⁴⁰ARCOptix, “Variable Spiral Plate (VSP) for vortex beams generation. (<http://www.arcoptix.com>),”.
- ⁴¹P. García-Martínez, D. Marco, J. L. Martínez-Fuentes, M. del Mar Sánchez-López, and I. Moreno, “Efficient on-axis slm engineering of optical vector modes,” *Optics and Lasers in Engineering* **125**, 105859 (2020).
- ⁴²X. Zheng, A. Lizana, A. Peinado, C. Ramirez, J. L. Martinez, A. Marquez, I. Moreno, and J. Campos, “Compact lcos-slm based polarization pattern beam generator,” *Journal of Lightwave Technology* **33**, 2047–2055 (2015).
- ⁴³Q. Zhan, “Cylindrical vector beams: from mathematical concepts to applications,” *Advances in Optics and Photonics* **1**, 1 (2009).
- ⁴⁴L.-C. Lin, H.-C. Jau, T.-H. Lin, and A. Y. Fuh, “Highly efficient and polarization-independent fresnel lens based on dye-doped liquid crystal,” *Optics Express* **15**, 2900 (2007).
- ⁴⁵J. Li, C.-H. Wen, S. Gauza, R. Lu, and S.-T. Wu, “Refractive indices of liquid crystals for display applications,” *Journal of Display Technology* **1**, 51–61 (2005).